Markerless lung tumor localization in cine MV images of deep-inspiration breath-hold IMRT treatments

Master's Thesis

Sky Rohrer

sky.rohrer@uzh.ch

Physik Institut, University of Zurich, Switzerland
Danish Centre for Particle Therapy, Aarhus University Hospital, Denmark

Supervisors:
Prof. Per Rugaard Poulsen
Dr. Jenny Bertholet
Prof. Peter Manser
Prof. Michael K Fix
Prof. Jan Unkelbach

June 19, 2022

Acknowledgements

I would like to express my warmest gratitude to Per Poulsen for inviting me to come to Denmark for this exchange to write my thesis and being an inspiring supervisor. After our meetings I always felt refreshed and motivated to get ahead on my project. He helped me gain a lot of experience in research and I especially appreciated the chance to present my work at ESTRO 2022.
Further, I would like to thank:
Jenny Bertholet for great guidance on the project, always having some motivating feedback and kind words, as well as connecting me to Per.
Peter Manser and Michael Fix for being so open to helping me find an exchange place and monthly follow-up meetings to ensure I was doing well.
My lovely friends and coworkers at DCPT for creating a welcoming and supporting work environment, in particular Villads Jacobsen and Imaiyan Chitra Ragupathy for helping me revise my writing and Simon N. Thomsen for answering all my questions.
Lone Hoffmann and Ditte Sloth Møller for letting me be part of their study on DIBH and always having great advice.
Simon Skouboe for providing the in-house code for generating the DRR.

I would also like to thank Nanna Steenholdt for the invaluable mental support whenever I needed it.

Lastly, I greatly appreciate the support from Science Alumni UZH and SEMP in the form of generous stipends that made my exchange possible.

Abstract

This study aims to investigate the reproducibility of deep inspiration breath hold (DIBH) in lung cancer patients treated with intensity modulated radiotherapy (IMRT), by using cine MV images. A method for markerless lung tumour localization was developed, which can be used to determine the intrafraction position error that occurs after the setup cone-beam CT (CBCT).

The method for markerless lung tumour localization in cine MV images was successfully developed and applied to 7 patients to determine the intrafraction tumour shift between setup imaging and treatment delivery in lung cancer DIBH IMRT treatments. Of the analysed treatments the tumour was deemed segmentable in 76% of IMRT fields containing the gross tumour volume (GTV) .

Positioning errors were determined by comparing the tumour position in the CBCT to the cine MV by template-based segmentation. The setup margins calculated from the positioning errors were between 3.8 and 5.5 mm in different directions. However, a significant systematic drift of 3.5 mm in the cranial direction was found, which is not yet accounted for in the clinically applied margins. This can lead to underdosage of the cranial end of the CTV.

Contents

Chapter 1

Introduction

1.1 Lung Cancer

This thesis will present data analysis of Lung cancer patients treated with Intensity-Modulated-Radiotherapy (IMRT) in Deep-Inspiration-Breath-Hold (DIBH).

In Denmark, lung cancer is the main cause of cancer-related deaths (25%) [1] and the five-year mortality rate for lung cancer is 65% [2]. Around 600 lung cancer patients are treated with radiotherapy every year in Denmark, ∼100 of which are treated at Aarhus University Hospital (AUH). Treatment of lung cancer with radiation is challenging due to a number of reasons such as anatomical changes during the treatment, breathing motion, as well as frequent late detection.

Radiotherapy is a non-invasive treatment that makes use of the physical interaction of radiation with matter. Most clinics use photon radiotherapy with external photon beams.

1.2 Photon-Matter Interactions

1.2.1 Photoelectric effect

Multiple types of reactions are possible between photons and matter (Figure 1.1), dependent on the photon energy and the absorbing material. For energies up to 1 MeV the photoelectric effect dominates, which is where a photon is absorbed by an electron in the shell of an atom and releases the electron carrying the energy of the photon minus the binding energy.

1.2.2 Compton scattering

The Compton effect is the most important in radiotherapy as it is the dominant reaction at the photon energy (∼6 MV) commonly used to irradiate patients (Figure 1.2). Here a photon is scattered inelastically on an electron of the outer shell,

thereby changing its direction, and losing energy. The lost energy is transferred to the secondary electron knocked from the atomic shell.

1.2.3 Pair production

Pair production only happens for photons with an energy above 1.024 MeV. The photon interacts with the nucleus's Coulomb field, creating an electron-positron pair. Therefore, the minimum energy of the photon needs to be at least 1.024 MeV, the rest mass of the secondary particles. The energy of the photon is completely transferred to the two particles, absorbing the photon in the process.

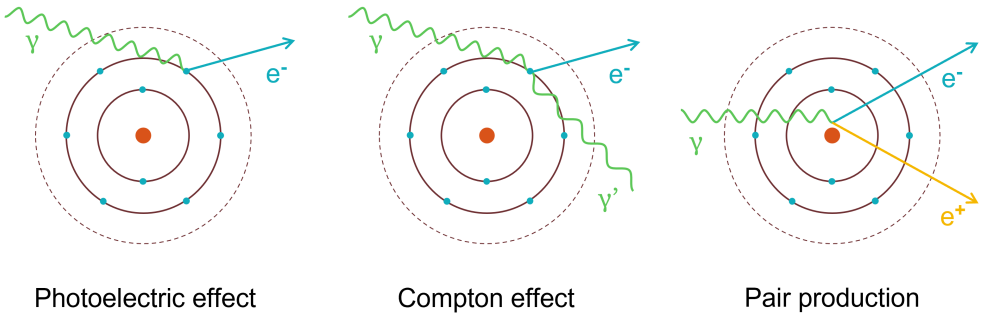

Figure 1.1: Illustration of the three most common photon-matter interactions based on Khan [3]

1.3 Dose deposition

If ionising radiation is applied to cells it ionizes the water molecules and the created ions can interact with the DNA strands and damage them. The goal of radiotherapy is to apply enough damage to the DNA in the cancer cells to either slow the growth of the tumour or even kill the cancer cells, depending on whether the intent of the treatment is curative. The absorbed dose D is defined by the energy dE deposited in a mass element dm, measured in Gray [Gy], where Gray has the units of Joule over kg.

$$D = \frac{dE}{dm} \tag{1.1}$$

$$[Gy] = \frac{[J]}{[kg]} \tag{1.2}$$

A photon beam is attenuated exponentially in matter, and the number of photons N at a given depth x in the absorbing material can be described as follows:

$$N = N_0 \, e^{-\mu x} \tag{1.3}$$

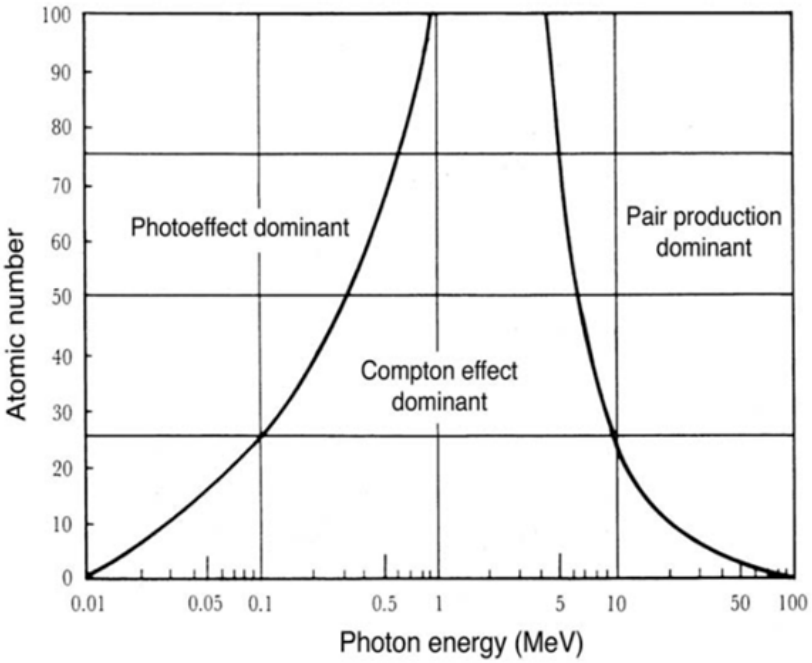

Figure 1.2: Regions of relative predominance of the three main forms of photon interaction with matter where the horizontal axis represents the photon energy, and the vertical axis the atomic number of the matter they interact with. The left curve represents the region where the atomic coefficients for the photoelectric effect and Compton effect are equal, the right curve is for the region where the atomic Compton coefficient equals the atomic pair production coefficient, adapted from Podgorsak [4]

N_0 is the total number of photons in the beam before it hits the absorber, μ describes the linear attenuation and is the composite of the linear attenuation coefficients of all possible interactions of the photons with the absorber.

Photons are considered indirectly ionizing radiation, as they are uncharged. The dose from photon beams is deposited through the secondary electrons that are produced when the photon is absorbed. This happens mostly via Coulomb scattering, where the electrons interact with other particles based on their charge, and hereby ionize the matter in their path, depositing dose. Since the electrons carry energy away from the interaction point in the forward direction, the dose at the entry point is reduced, leading to a skin-sparing effect. This can be seen in the depth-dose curve where PDD is the percentage depth dose relative to the maximum (Figure 1.3).

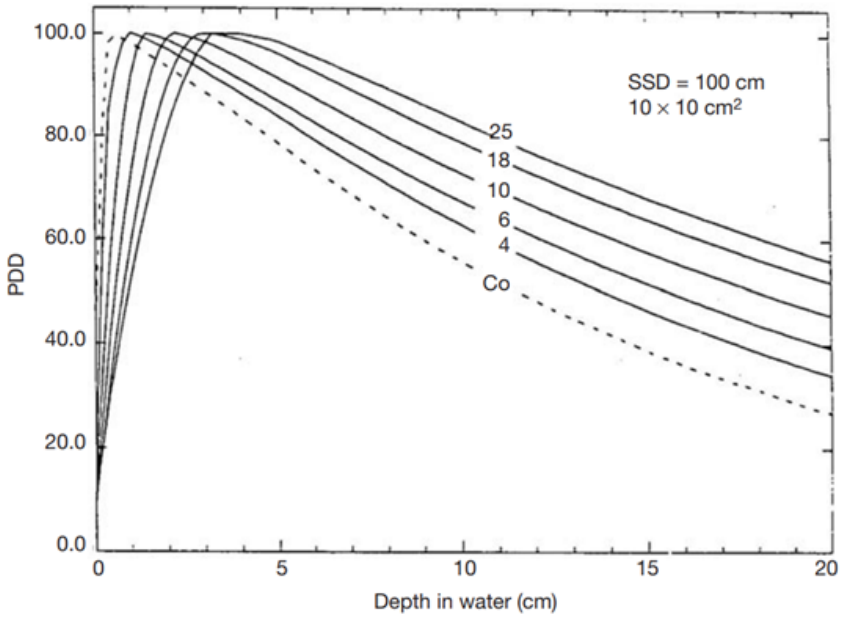

Figure 1.3: PDD curves for Cobalt (Co) and photon energies from 4 - 25 MV in water for field size = 10x10 cm^2 source to surface distance (SSD) = 100 cm, adapted from Podgorsak [4]

1.4 Radiotherapy in the Clinic

1.4.1 Imaging

For diagnostic and planning purposes, imaging is essential. In the clinic, this is mostly done using photons (X-Rays). When imaging with photons, the photoelectric effect is central. Since its cross-section heavily depends on the atomic number of the different tissues, this allows seeing structures with heavier elements in the body, such as bones. This can be done from one angle, resulting in a 2D projection image through the entire body, or from multiple angles at once which can be used to compute a 3D image of the patient: This is called computed tomography (CT). Here the patient is imaged from all angles, resulting in multiple projections through the patient. These are then back-projected to estimate the 3D anatomy. The more projections are taken, the more precise the back projection gets.

Two types of CT are used in the planning and treatment process of a patient in radiotherapy. At the beginning (Figure 1.4), a planning CT (fan-beam CT) of the patient is taken. This is done slice by slice, where the source and detector rotate around the patient in a helix motion to cover the cranio-caudal (CC) direction. During the treatment, a setup Cone-Beam CT (CBCT) is taken to set the

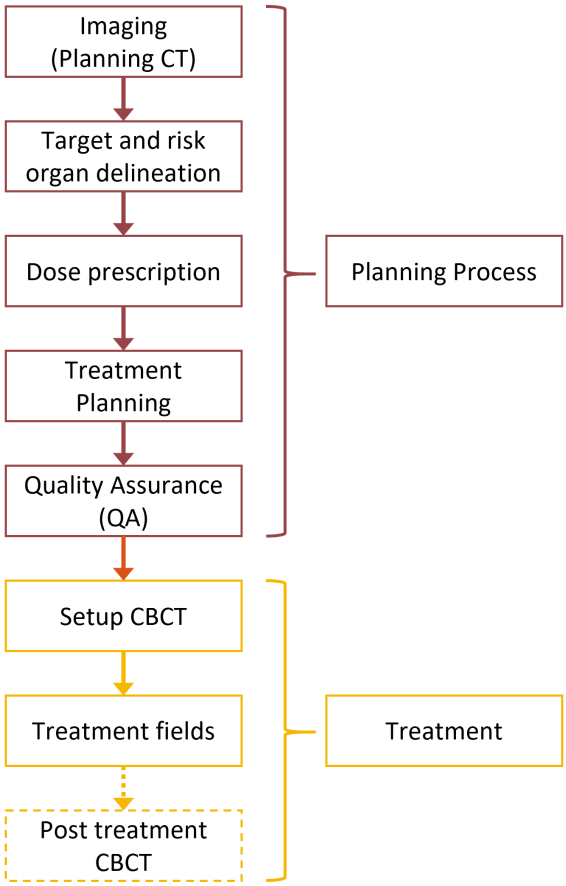

Figure 1.4: Planning and Treatment Process in the clinic

patient up for treatment in the correct position (in some cases a second CBCT is taken after treatment delivery to investigate the intrafraction motion). Here the source and detector only rotate around the patient *once*. In this modality, the source produces a cone beam that covers the entire imaged area at once to save time, since the source can only rotate at a slow speed.

The different ways of acquiring the projections cause a considerable difference in quality between the two modalities. CT usually covers a bigger volume and the fact that the image is taken row by row eliminates most of the noise created by scattered photons. Contrastingly, taking the entire image at once with a big field gives rise to a lot of scattering that negatively impacts the quality of a CBCT scan compared to a CT scan. Additionally, motion artefacts are much more severe in CBCT scans, due to the long acquisition time.

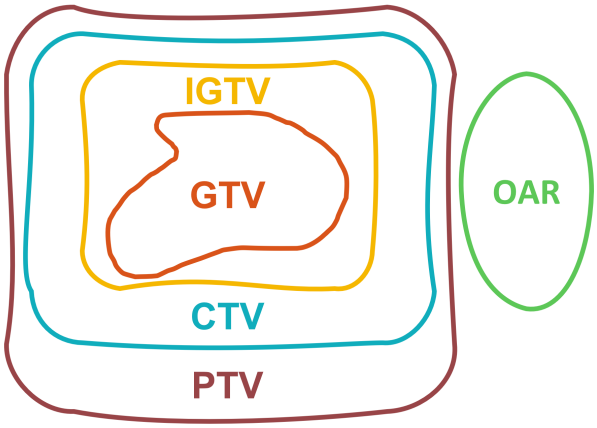

Figure 1.5: Delineated structures

1.4.2 Target delineation

A crucial part of treatment planning is delineation on the planning CT: identifying the tumour and organs in the patient and defining the targets for radiotherapy. The following describes the procedure at AUH for lung cancer patients treated in DIBH:

The Gross Tumour Volume (GTV) is the target structure that is visible on the CT scan (Figure 1.5). This can be the lung tumour or lymph nodes that are to be irradiated. The GTV is delineated in 4 planning DIBH CT scans taken in succession. Due to internal motion, such as variation in the depth of the breath-hold, these four GTVs may not be in the same position. Therefore, to compensate for this uncertainty, margins are added. The Internal GTV (IGTV) is formed by enveloping the volume of all four GTVs to incorporate the internal target motion. This results in patient-specific margins.

The Clinical Target Volume (CTV) is the IGTV expanded to the subclinical microscopic spread of the tumour cells into the surrounding healthy tissue. A 5mm margin is used in all directions and cropped to bones and large vessels.

The Planning Target Volume (PTV) is the CTV extended with predefined margins based on the type of tumour. The hospital uses 4 mm in left-right (LR) and anterior-posterior (AP), 5 mm in CC direction for the lung tumour targets, and 7mm and 8mm respectively for lymph node targets. The aim of adding the margins is to account for uncertainties in the setup and systematical errors, which would negatively impact the accuracy and therefore treatment outcome if not considered.

Further, the organs at risk (OAR) are delineated, this includes for example the heart and the spinal cord. After delineation, the dose to the targets and the number of fractions is defined by a radiation oncologist, including the maximum dose to the OAR. This is important so they can be protected from high doses that would impact their functionality and therefore quality of life for the patient.

1.4.3 Treatment planning

Treatment planning is an optimisation process, as it is difficult to assure prescribed dose coverage of the PTV while sparing the OAR. Due to the exponential decline of the dose with depth for photon beams (Figure 1.3), patients are irradiated with multiple fields from different directions. The fields overlap in the region of the PTV, therefore cross-firing the tumour and adding up to the prescribed dose, while the healthy tissue outside of this region is exposed to a lower dose.
Before the patient is treated, Quality Assurance (QA) is done to ensure that the planned treatment is accurate. On the one hand, the plan is recalculated with an independent Monte Carlo algorithm to ensure the planned dose distribution is reproduced. On the other hand, the IMRT fields are delivered to a fluorescence plate where the deposited dose is measured and compared to what was planned. This ensures correct movement of the MLC leaves.

1.4.4 Treatment

The photon fields for the treatment are administered by a linear accelerator (LINAC). It can produce photons with energies up to 15 MV by accelerating electrons that are then directed onto a target, where photons are created by Bremsstrahlung and then collimated to form the photon beam. For this study, patients were treated with 6 MV photons. In this context, 6 MV stands for the voltage used to accelerate the electrons and describes a photon energy *spectrum* with a maximum of 6 MeV. The Linac treatment head (gantry) can be rotated around the patient and deliver multiple fields from different angles to create the desired dose distribution.

1.4.5 Intensity Modulated RadioTherapy (IMRT)

To get an optimally conformal dose distribution to the PTV, IMRT is applied. It allows for delivery of an inhomogeneous field dose, for example, a lower dose on lymph nodes and OAR and a higher Dose on the PTV. This is achieved most commonly by using Multi-Leaf Collimators (MLC) to shape the photon beam. MLC consist of multiple leaf pairs that can be positioned individually, usually made from tungsten alloy. Those leaf pairs can now shape a beam conformal to the tumour (Figure 1.6) and can also be moved while the beam is on and cover

the field in a sliding-window method. Areas that are exposed for longer time therefore get higher dose. The movement of the MLC is optimized in treatment planning.

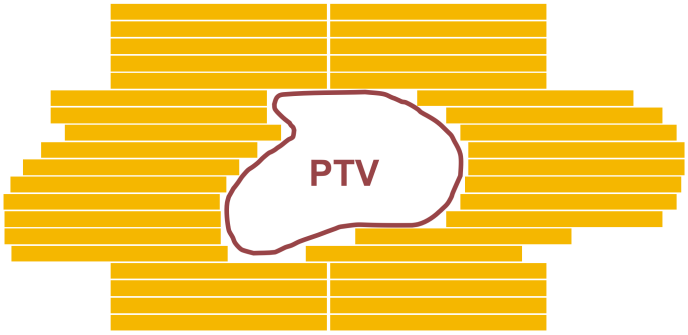

Figure 1.6: An example of a conformal aperture to the PTV in beams eye view, shaped by the MLC leaves (yellow)

1.4.6 Image-Guided RadioTherapy (IGRT)

After the careful planning of the optimal dose distribution, it is crucial to have a way to ensure that the patient is positioned exactly according to the treatment plan. On the Linac there are two possibilities to image the patient and get more accurate information about the geometry than from markers on the skin.

Firstly, there is a kV imager perpendicular to the gantry. It can take CBCT for setup, as well as 2D images during treatment. For the setup, a match on the main tumour is made between the CBCT and the planning CT, the couch is then adjusted according to the match.

Secondly, an electronic portal imaging device (EPID) is in line with the gantry underneath the Patient. It can record the MV photons that pass through the patient during the treatment (cine MV images). This may be used to verify the shape of the beam and placement relative to the isocentre are correct. The tumour may also be visible in those images; however, the contrast is much less distinct than in kV images such as CT scans. This due to the lack of the photoelectric effect at the photon energies used for treatment. These images will be analysed in this thesis.

1.4.7 Motion management

Lung tumours are particularly difficult to treat when it comes to motion management. During a free-breathing cycle, the target can move up to several cen-

timetres. To counteract this, large margins must be added, resulting in a high dose to healthy tissue and therefore high toxicity, about 1/3 of patients develop symptoms of radiation pneumonitis [5, 6]. Gating is often used to reduce the target motion during treatment, where the beam is only on when the tumour is in a specified range.

A way to mitigate tumour motion is DIBH. For DIBH the patient breathes in deeply and then holds their breath for about twenty seconds at a time, during imaging and treatment. The breath-hold is monitored via a marker block placed on the patient's chest and an infrared camera tracking its position. The beam is gated to only be ON during the breath-hold.

Additionally, lymph node markers are implanted, that can be tracked via the kV imager integrated in the LINAC. Analysing their motion can be helpful to understand the intrafraction motion of the tumour better but the two do not directly correlate, since the lymph nodes may not be right next to the tumour.

The advantages of DIBH are several: by expanding the lung, the distance between OAR and PTV may be increased, as well as reducing the density of the surrounding normal tissue. Therefore, radiotherapy treatment in DIBH reduces intrafraction tumour motion, while also reducing the mean lung dose, and it may even reduce the dose to OAR such as the heart [7] depending on the geometry. Additionally, the imaging quality in planning CT and setup CBCT is much improved compared to scans in free-breathing, as there are fewer motion-based artefacts. However, as the CBCT is taken in 3 DIBH cycles of 20 seconds each, residual motion can't be entirely eliminated.

At AUH, lung cancer patients with a target movement of over 8 mm during a breathing cycle are treated in DIBH if possible. This only applies to a small number of patients, between 2017 and 2022, only 29 of $\sim$500 patients were treated in DIBH.

1.5 Aim

The targeting accuracy of DIBH treatment can be compromised through poor correlation between the external gating signal and the internal target position. Until now it has not been possible to directly assess the tumour location during irradiation. The available information was limited to the setup CBCT before and in some cases after the treatment, as well as imaging and tracking of the implanted lymph node markers in kV images during the treatment.

Therefore, this study aimed to investigate the reproducibility of lung DIBH using template-based segmentation for markerless lung tumour localisation in cine MV images during IMRT delivery. The developed method can be used post-treatment to determine the tumour intrafraction motion positioning error that occurs between the setup CBCT scan and the treatment.

Chapter 2

Materials and Methods

2.1 Dataset

The patient cohort for this study consists of 29 lung cancer patients treated in DIBH at AUH from 2017 to 2021.

Thirteen patients with Non-Small Cell Lung cancer (NSCLC) were treated with 66 Gy to the PTV in 33 fractions with 5 fractions per week. Ten patients with NSCLC were treated with 50 Gy to the PTV with dose escalation to the GTV in 24 fractions with 5 fractions per week. This was done when the dose restriction to the OAR was exceeded with 66 Gy to the PTV. Six patients were diagnosed with Small Cell Lung Cancer (SCLC) and treated with 45 Gy in 30 fractions total with 10 fractions per week. Out of those patients, seven were analysed as part of this study due to time constraints. One was diagnosed with SCLC and the remaining six had NSCLC.

	Cohort	Analysed
NSCLC	23	6
SCLC	6	1

Table 2.1:

The following data was available for the patient cohort:

- DIBH planning CT (512x512x189 voxel, 1.17x1.17x3 mm^3)
- DICOM Plan file
- DICOM Structure File
- CBCT setup scan for every fraction (512x512x185 voxel, 0.88x0.88x3 mm^3)
- Setup couch shift for all fractions

- Cine MV images for 80% of fractions taken with a frequency of 7.5 Hz (768x768 pixel, 0.39x0.39 mm^2)
- Second CBCT after treatment for fractions 1, 2, 3, and then weekly

2.2 Workflow and Algorithm for markerless tumour localisation

This section describes the algorithm that was developed to analyse the cine MV images, this was done in MATLAB [8]. Figure 2.1 describes the workflow:
Cine MV images are taken while the MLC move over the field, only exposing parts of it at once. Ideally, DIBH has no residual tumour motion, therefore, the individual cine MV frames of the IMRT treatment could be pieced together to form a composite cine MV image (Section 2.2.1).
Next, an in-house developed ray-tracing algorithm was used to generate digitally reconstructed radiographs (DRRs) based on the entire CBCT (DRR_{total}), a slab of the CBCT containing the tumour volume (DRR_{tumour}), and the entire CBCT except for the tumour containing slab ($DRR_{non\text{-}tumour}$) (Section 2.2.2).
All DRRs were rescaled to have similar contrasts as the composite cine MV image (Section 2.2.3). $DRR_{non\text{-}tumour}$ was then subtracted from the composite cine MV

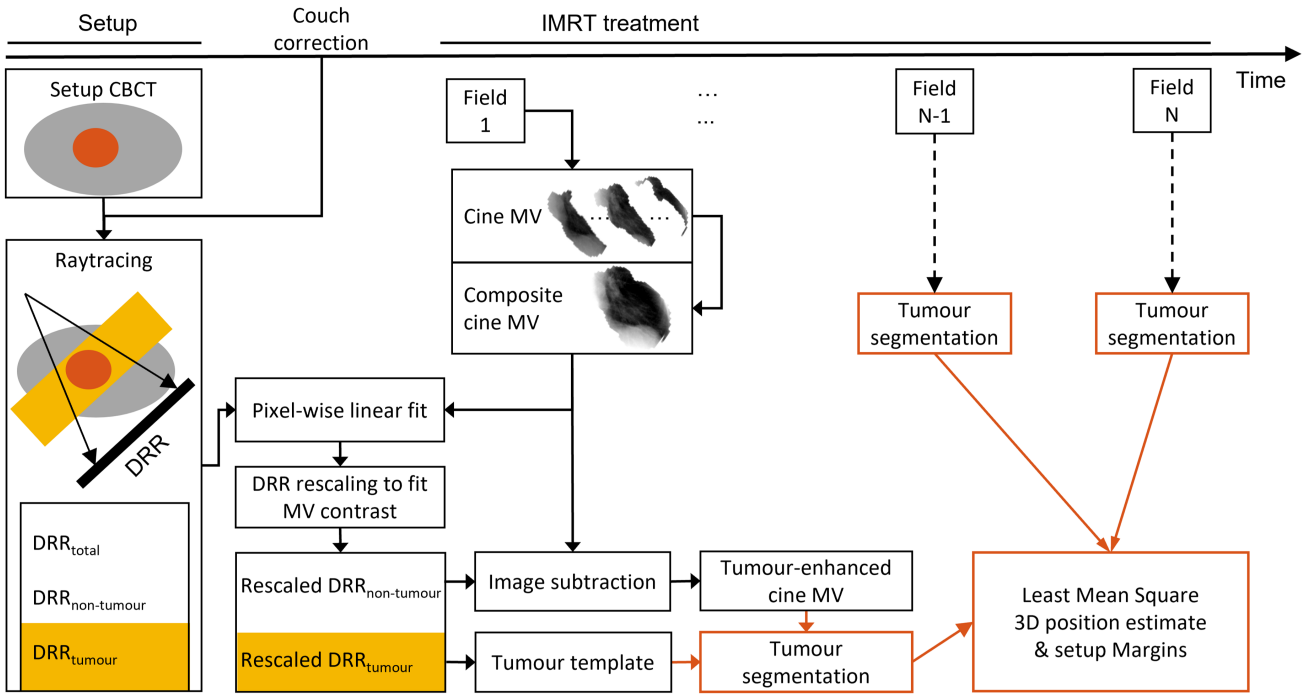

Figure 2.1: Flowchart describing the algorithm

image to generate a tumour-enhanced cine MV image (Section 2.2.4) in which the tumour position was found by template-based segmentation using the projected tumour shape in DRR_{tumour} as a template (Section 2.2.5).
This is repeated for all segmentable fields, after which a least mean square method was used to estimate the 3D position of the tumour during treatment (Section 2.2.6) and then calculate setup margins (Section 2.2.7).

The following sections describe the individual steps in the analysis in more detail:

2.2.1 Generating the composite image

The first step in the process was stitching together the cine MV images into a composite image under the assumption that there was no tumour movement during the DIBH. Since the treatment was intensity-modulated, the MLC leaves sweep over the field during irradiation. This causes the cine MV images to be exposed to only parts of the entire field at a given time (Figure 2.2), therefore, the tumour shape can not be segmented in the individual frames. To generate an image of the full aperture, for each field in each fraction separately, a composite MV image (cMV) was created where every pixel is assigned the value from the cine MV frame where it is most exposed (Figure 2.3 a). Generating a high-quality composite image was possible due to the DIBH, as this results in minimal tumour motion during a breath-hold cycle. However, if the field was delivered in two breath holds, it was not possible to produce a motion artefact-free cMV image.

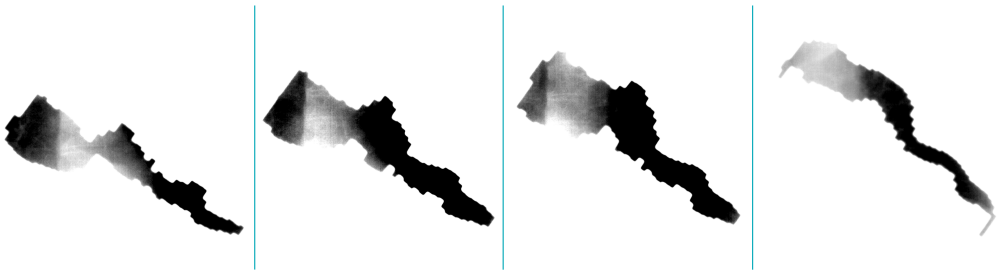

Figure 2.2: individual cine mV images showing the sliding-window motion of the MLC from the beginning of the field (left) to the end (right) taken from Patient 4, Field 6

This method for generating the composite works well for most cine MV files, however, in some cases, there were artefacts. When calculating the mean intensity of each cine MV frame of an irradiated field, it became apparent that the frame rate of the frame grabber was not perfectly stable which caused some frames to be over-and underexposed relative to the other frames in the cine MV series (Figure 2.3 c). When disregarded, this caused significant artefacts in the cMV images, to an extent where segmenting the tumour became impossible (Figure 2.3

b).

For most fractions, the following method was useful to smooth out the image: From the mean intensity of each image, outliers, most importantly maxima, could be identified and flagged. These frames were not included in the composite images. The criteria to single them out have been chosen empirically:

- Exposure of frame i is more than 1.2 times the exposure of frame $i-1$
- Exposure of frame i is more than 1.2 times the exposure of frame $i+1$
- Exposure of frame i is more than 1.6 times the exposure of frame $i-3$ and more than 1.1 times the exposure of frame $i+1$
- Exposure of frame i is more than 1.6 times the exposure of frame $i-2$ and more than 1.1 times the exposure of frame $i+1$
- Exposure of frame i is higher than both, the exposure of frame $i-1$ and the exposure of frame $i+1$

After those frames have been excluded, most composite images are free of artefacts (Figure 2.3 d). The remaining images where this is not the case were manually corrected to exclude the additional disturbing frames.

Further methods that were explored to generate artefact free composite images but were not sufficient to eliminate the artefacts:

- Normalisation of all images using the overall mean intensity of the cineMV stack
- Find local minimal and maxima in the intensity. If they are immediately following each other, average the two and replace both images in the stack with the average.
- Using the built-in outlier function in MATLAB. This function was oversensitive in some cases and not sensitive enough in others.

2.2.2 Generating Digitally Reconstructed Radiographs (DRR)

To be able to compare the two-dimensional cine MV images to the setup CBCT, which is 3D data, part of the in-house algorithm Dose Tracker [9] was used to calculate a projection of the CBCT volume from the gantry angle to the imager plane. This type of projection is called a Digitally Reconstructed Radiograph (DRR) and is a 2D projection based on the 3D image volume of the CBCT converted from Hounsfield units (HU) to density. The DRR is projected by ray tracing from the source, through the image volume to every pixel in the imager. The densities are then added up along each ray, resulting in water equivalent

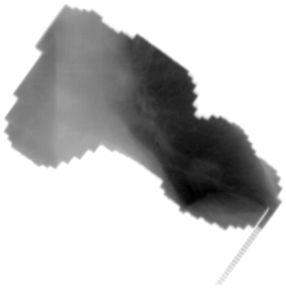

(a) Fraction 14: composite with optimal exposure

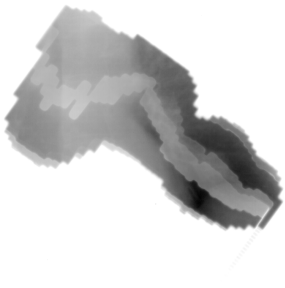

(b) Fraction 21: composite with exposure artefacts

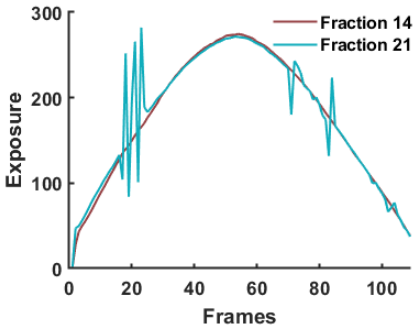

(c) Exposure for a and b

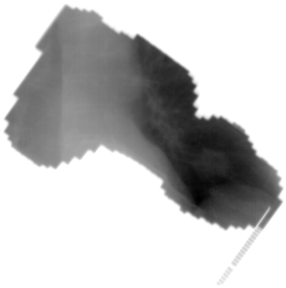

(d) Fraction 21: composite with exposure artefacts removed

Figure 2.3: Examples for MV images taken from Patient 4, Field 6

path length (WEPL) for each pixel.

To calculate the DRRs, the treatment plan and structure file were imported as a Dicom file, to read the field sequence, gantry angles, the isocentre and tumour position. Further, the online couch shift from the setup match is imported so the image volume can be shifted accordingly to match the patient position during the treatment.

In a first step, the CBCT resolution was refined by interpolation from 3 to 1 mm in the CC direction and then the voxels were converted from HU to density.

$$\rho = \frac{HU + 1000}{1000} \tag{2.1}$$

With the imager span and the resolution of the EPID known, the DRR was calculated by ray tracing. A Gaussian filter with a standard deviation of 2 was

then applied to the resulting image for smoothing. For every field in a fraction 3 DRRs were calculated:

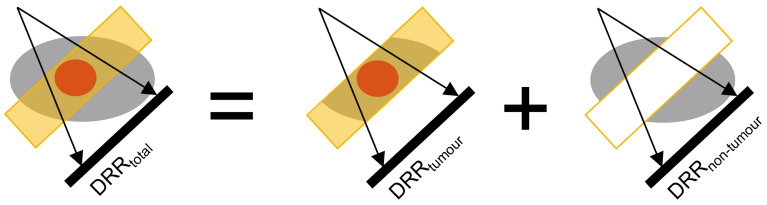

Figure 2.4: the generated DRRs

DRR_{total}:	DRR of the entire CBCT volume
DRR_{tumour}:	DRR of a slab perpendicular to the beam containing the tumour volume (thickness of the slab was defined by the width of the GTV without additional margins)
$DRR_{non\text{-}tumour}$:	DRR of the entire CBCT volume except for the tumour-containing slab

Where DRR_{tumour} (Figure 2.5 c) and $DRR_{non\text{-}tumour}$ (2.5 b) add up to DRR_{total} (2.5 a). The two partial DRRs were made for enhancing tumour contrast later, taking advantage of the three-dimensional information available.

2.2.3 DRR rescaling

At this point of the analysis, a cMV image (Figure 2.5 d) and 3 DRRs are available for every field and fraction. Since photons of different energies are used to acquire the images, the respective tissue contrast in the cMV and the DRRs is very different. The CBCT has been imaged with 110 kV photons, making use of the contrast created due to the photo electric effect. This effect is no longer significant when using MV energy photons (6 MV) as used in photon therapy. There the Compton effect dominates, where the attenuation coefficient is proportional to the density of the tissue only, which leads to less contrast in the images.

To enhance the tumour contrast in the cMV image, the intensities must be similar for various tissues in all modalities. Therefore, the DRRs were rescaled to obtain intensities similar to the cMV. This intensity normalisation was achieved by making a pixel-wise linear fit on the WEPL of the DRR_{total} and the cMV within the MLC aperture. Additionally, the size of the CBCT scan had to be considered, since the MLC field size can be larger than the size of the scan in the CC direction. The MLC aperture for each cMV was found by looking only at pixels below a certain intensity (80% of the max intensity) which gave an ac-

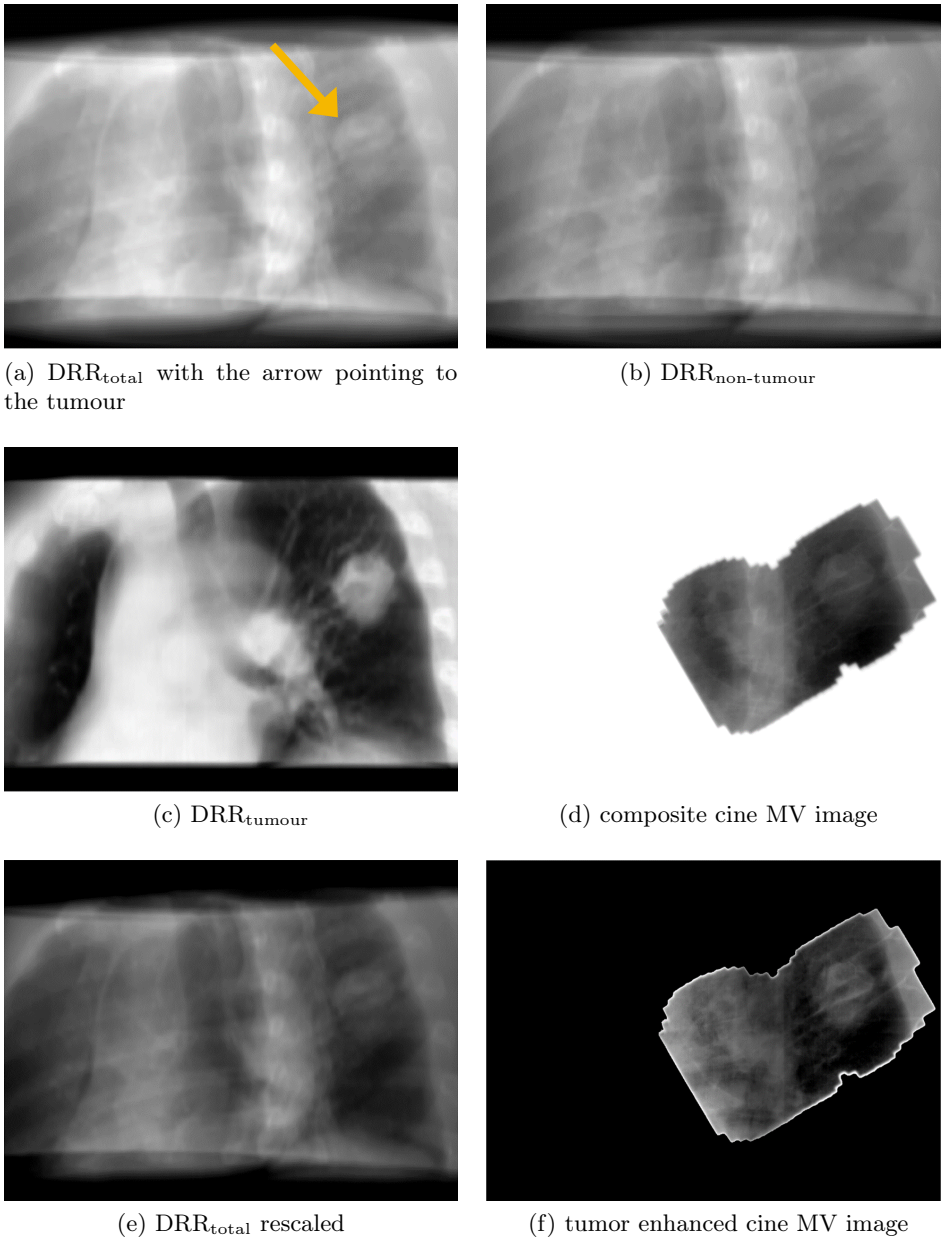

(a) DRR_{total} with the arrow pointing to the tumour

(b) $DRR_{non\text{-}tumour}$

(c) DRR_{tumour}

(d) composite cine MV image

(e) DRR_{total} rescaled

(f) tumor enhanced cine MV image

Figure 2.5: Examples for processing DRRs and MV images taken from Patient 6, Field 4

curate mask without having to use the structure file. Figure 2.6 shows such a pixel-wise linear fit. The horizontal stripes visible in the scatter plot below the linear fit are due to the residual penumbra from the aperture on the cMV. This linear fit was used to rescale all pixel values in the three DRRs (Figure 2.5 e).

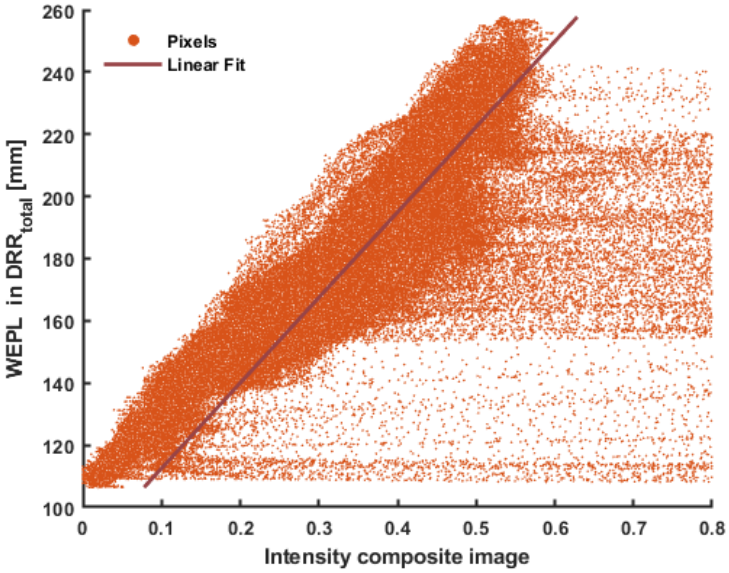

Figure 2.6: Pixel values for composite MV and DRR and the linear fit, where the horizontal axis corresponds to the pixel values in Fig. 2.5 d) and the vertical axis corresponds to the pixel values in Fig. 2.5 a), taken from Patient 6, Field 4

2.2.4 Tumour-enhanced composite MV image (teMV)

Generating a tumour enhanced composite MV (teMV) image is crucial, since the tumour often has low contrast in cine MV images compared to other tissues, such as bones or the heart, and may be covered by ribs. This makes the template-based search difficult, therefore the goal is to reduce the intensity of structures that are not of interest or in the way by subtraction.
Since $DRR_{\text{non-tumour}}$ contains most of those structures, it is used for the subtraction. However, to calculate the subtraction, the intensities of the two images need to be proportional to the same physical property. The intensity of the pixels in the rescaled DRR is proportional to the integral of the density along the path since it is based on the calculation of the WEPL.
The cMV image with intensities from 0 to 1 is a measure of the number of photons per pixel where 1 (white) corresponds to zero photons and 0 (black) corresponds to the maximum number of photons per pixel. Since the attenuation coefficient μ in Eq. (2.4) for the Compton effect is proportional to the density integrated over the path (2.5), the logarithm of the pixel intensities $+1$ are proportional to the integrated density (2.6).

Therefore, the teMV image (Figure 2.5 f) was calculated according to Eq. (2.7) where teMV, cMV and $DRR_{\text{non-tumour}}$ each stand for the intensity of a pixel in the corresppponding image. The minimum pixel value was set to zero.

$$\begin{aligned}
\mathrm{DRR}_{\text{non-tumour}} &\propto \int \rho(x)\,dx && (2.2)\\
\mathrm{cMV} &\propto -\frac{N}{\text{pixel}} && (2.3)\\
N &= N_0\ e^{-\mu x} && (2.4)\\
\mu_{\text{compton}} &\propto \int \rho(x)\,dx && (2.5)\\
\log(1+\mathrm{cMV}) &\propto \int \rho(x)\,dx && (2.6)
\end{aligned}$$

$$\mathrm{teMV} = \log(1+\mathrm{cMV}) - f \cdot \mathrm{DRR}_{\text{non-tumour}} \quad (2.7)$$

A subtraction factor f was included to adjust to the optimal tumour contrast for each field individually. In cases where structures with high contrast, especially the diaphragm, had moved between the setup CBCT and the field delivery, subtraction caused prominent shadows. This was mitigated by manually adjusting the subtraction coefficient since these artefacts may complicate the template-based search. On average, a subtraction coefficient of 0.67, found through iteration, worked well for most fields and fractions.

2.2.5 Tumour template and segmentation

With the enhanced tumour contrast in the teMV image, normalised cross-correlation can now be used to find the difference in tumour position. The shape of the GTV delineated on the planning CT can be extracted from the plan structure file and projected into beam eye view as a mask. Since the setup CBCT has been shifted to align with the planning CT according to the match made before the treatment, the tumour structure should be found within that mask. Therefore, the mask is now used to cut a tumour template from the $\mathrm{DRR}_{\text{tumour}}$. This can be done in two ways: Either the extent of the structure is used to cut a rectangular template from the $\mathrm{DRR}_{\text{tumour}}$, or the mask is used directly to generate an irregularly shaped template conformal to the GTV shape. In cases of tumour shrinkage from planning CT to treatment, the template was manually adjusted to be smaller. This prevented the algorithm from basing the template match on structures outside the tumour.

To segment the tumour position, the template is first placed in the same position on the teMV image as in the DRR, representing the expectation without any shifts occurring. The cross-correlation coefficient is then calculated for all

positions within a search window of ±60 pixels in vertical and ±40 pixels in horizontal direction of the imager, corresponding to ±15.7 mm and ±10.4 mm respectively with a pixel size of 0.261mm^2 at the isocentre. The position with the highest correlation coefficient is returned from which the tumour shift can be calculated relative to the intended tumour position in the CBCT. Figure 2.7 shows the rectangular template in the $\mathrm{DRR}_{\mathrm{tumour}}$ and where it was found in the teMV image

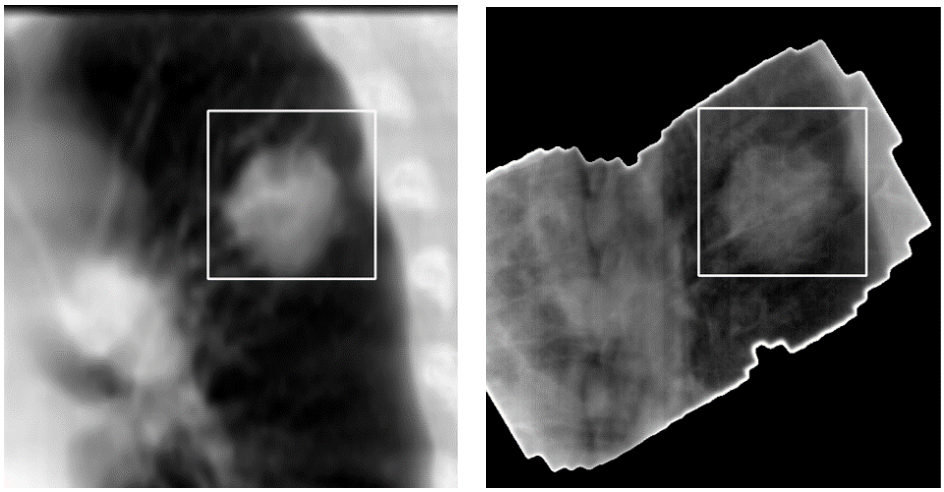

(a) Template in $\mathrm{DRR}_{\mathrm{tumour}}$

(b) Template segmented in tumour enhanced MV image

Figure 2.7: Example for template-based segmentation of the tumour, taken from Patient 6, Field 4

Since the built-in cross-correlation function in MATLAB (`normxcorr2`) can only handle rectangular templates, a new function had to be written that could compare templates cut with an irregularly shaped mask. This was done by assigning the pixel values within the mask to two vectors: One for the template and one for the region in the composite image over which the template has been placed. Those can now be compared directly. This is repeated for all the possible template positions within the region of interest in the teMV image and again, the highest correlation value corresponds to the found tumour position.

The template-based segmentation worked well for most tumour positions, except where the GTV was close to the diaphragm. This was the case in two fields for both patients 1 and 4. Due to the gating signal not correlating directly to the diaphragm position during repeated DIBH, the diaphragm position in the MV images varied from its position in the CBCT. Due to the high contrast between

the diaphragm and lung tissue compared to the contrast to the tumour, this increases the difficulty of finding tumour structures overlapping with the diaphragm in the teMV image.

An approach to refine segmentation for these cases included determining the diaphragm shift between the CBCT and the MV image and adjusting the section containing the diaphragm in $DRR_{non\text{-}tumour}$ for the subtraction accordingly. However, it remained difficult to get an artefact-free subtraction of the diaphragm shape due to the diaphragm being a non-rigid structure and therefore the benefits of this method were not sufficient to include it in the final version of the algorithm.

For a qualitative validation, the template-based segmentation the DRR template and its MV counterpart were normalized to the same grayscale, and an overlay, as well as a side-by-side comparison, were made (Figure 2.8). For each patient, the segmentations of all fractions were then verified visually and if necessary, the segmentation algorithm was refined. This worked well unless the appearance of the tumour in the DRR and the MV images was very different, in these cases it was not possible to verify the segmentation. This illustrates the complexity of the segmentation, as there was no ground truth that could be used as a control reference.

2.2.6 3D position estimation

Having segmented the tumour position for multiple fields and therefore multiple angles during a fraction, a 3D position estimate can now be calculated for each fraction. This estimate supplies a measure for the overall shift and setup precision during the treatment, which proves more robust than looking at the individual breath-hold cycles and allows for margin calculation in all three dimensions.

The method requires the gantry angle for each segmented field and the tumour's respective relative vertical and lateral positions in the imager plane, as well as the source to axis distance (SAD) which was 100 cm. The segmented positions are back-projected for each gantry angle relative to the isocentre (Figure 2.9) a). The lines represent the SAD from the MV imager source position to the segmented tumour position on the isocentre plane. Then the 3D position is estimated using an iterative least mean square optimisation to minimize the distance of the estimated position perpendicular to the projected SAD lines represented by the coloured lines in Figure 2.9 b. In the CC direction the estimated position is roughly the mean over all fields.

To calculate the errors relative to the segmented positions, the difference in distance is scaled by a factor that corrects for distance from the isocentre. This

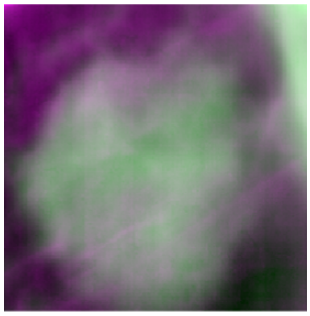

(a) Fraction 2 overlay

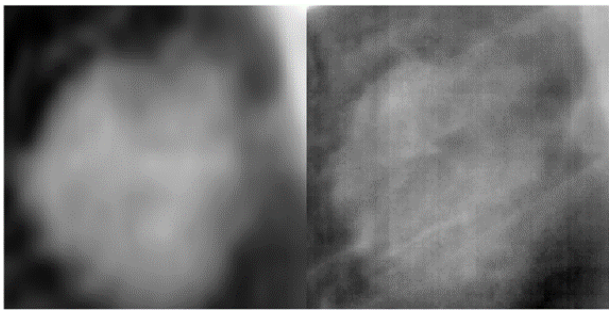

(b) Fraction 2 montage

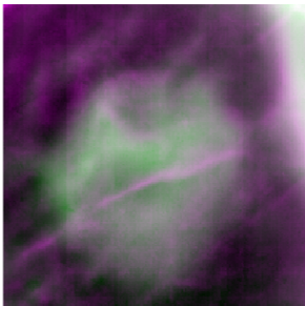

(c) Fraction 13 overlay

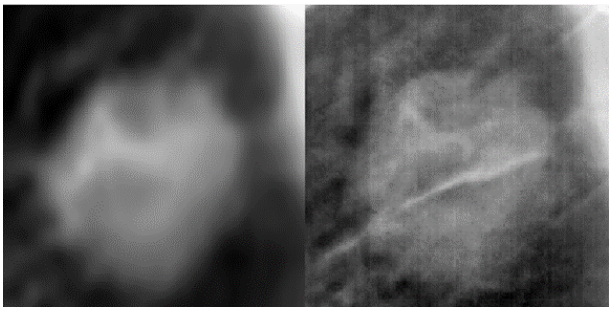

(d) Fraction 13 montage

Figure 2.8: Patient 6 Field 4: Overlays and montage of the template from DRR_{tumour} (left) and the template segmented in the teMV image (right)

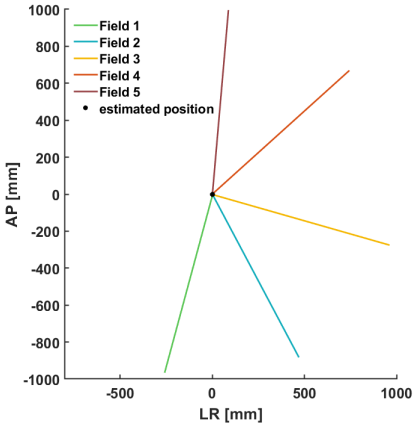

(a) back-projection of segmented positions projected along the gantry angles

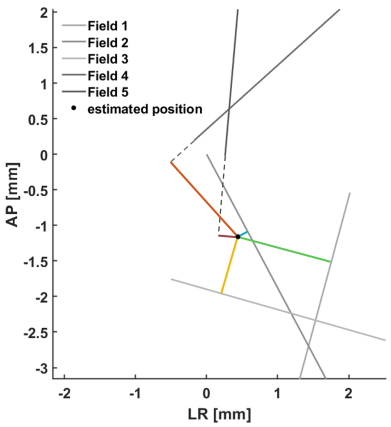

(b) closeup of (a) showing the estimated position and coloured lines representing the minimised distances

Figure 2.9: Axial view of 3D position estimation with five fields

is necessary due to the nature of the projection: objects closer to the imager appear smaller than if they are further away (see Figure 2.10) and the segmented positions were scaled according to the pixel size at the isocentre. From this, the root mean square (RMS) error can be determined as a measure of uncertainty.

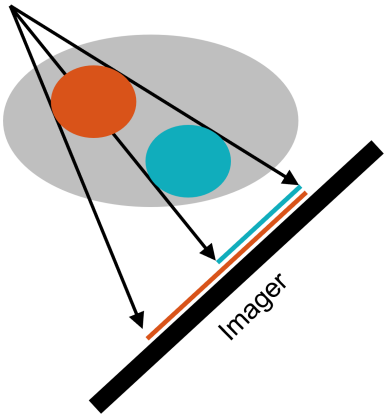

Figure 2.10: The size of an object in the projection depends on its distance from the imager

2.2.7 Setup Margins

During both the planning and treatment phase, numerous error sources impact the accuracy of the treatment and negatively impact the dose distribution. To ensure that the planned dose is delivered to the CTV, safety margins are needed. To compare the PTV margins used in the clinic to the tumour positions found in this study, margins were calculated from the patient data. The uncertainties can be separated into two categories: Random errors and systematic errors. Random errors are different for every field and/or fraction and therefore cause a blurring of the dose distribution. An example of this is respiratory motion. Systematic errors have a much graver impact on the dose distribution, as they cause a shift in the dose distribution and large parts of the CTV may end up underdosed if not corrected for. Poor correlation between the internal target position and the external gating signal and drifts in organ positions are examples of this. In conclusion, systematic errors must lead to bigger PTV margins than random errors.

Margins were then calculated according to van Herk [10, 11]:
For each patient n the mean M_n and the standard deviation σ_n (SD) were calculated from the estimated 3D positions. Then, Σ was calculated as the SD over the individual means and σ was calculated as the RMS of the individual σ_n. The population mean M was calculated as well, and then the PTV margins in all

three dimensions were determined according to equation 2.10.

$$\Sigma = \mathrm{SD}(M_n) \tag{2.8}$$
$$\sigma = \mathrm{RMS}(\sigma_n) \tag{2.9}$$
$$\text{Margin} = 2.5\Sigma + 0.7\sigma \tag{2.10}$$

Where Σ now represents the systematic errors and how reproducible the treatment setup is, σ represents the random errors of the population. The coefficients for the setup margins are designed to ensure that 90% of patients receive a minimum cumulative CTV dose of 95% of the prescribed dose if the distribution is shifted to be centred around zero.

2.3 Further methods to analyse data

2.3.1 Interfraction variation

Since the tumour placement in the setup is based on the radiation therapist's (RTT) match, this adds a subjective component to the process. In the method described above, only the reproducibility of this position was investigated. The following method describes an attempt to investigate the interfraction variation per field and relate the tumour position in the cMV images to either the first setup CBCT or the planning CT. This was done for each field seperately, by comparing the teMV images of the fractions directly to each other instead of using the daily setup CBCT as a tumour template:

For the first fraction, the tumour was segmented as described in Section 2.2.5, returning the relative position of the tumour to the setup. Since this segmentation finds the tumour template in the teMV image, this can now be used as a tumour template for the next fraction. For the second fraction and on, the teMV is calculated. Then, the tumour is segmented using the teMV image of the previous fraction as a template and the position is calculated relative to the previous fraction. This can then be related back to the first template that was used, in this case the first setup CBCT.

However, this method was unstable and had a lot of drawbacks: It could not handle the aperture edge being in the frame, as overlaying the two images to match there, gave the biggest cross-correlation (Figure 2.11), as well as having difficulties handling tumour shrinkage or inconsistent sizes of the tracked objects: the algorithm would match the pictures to overlap at one edge of the tumour, with inconsistency as to which edge that would be. This caused drifts in the template/found positions that defeated the purpose to go from a relative position to an absolute one.

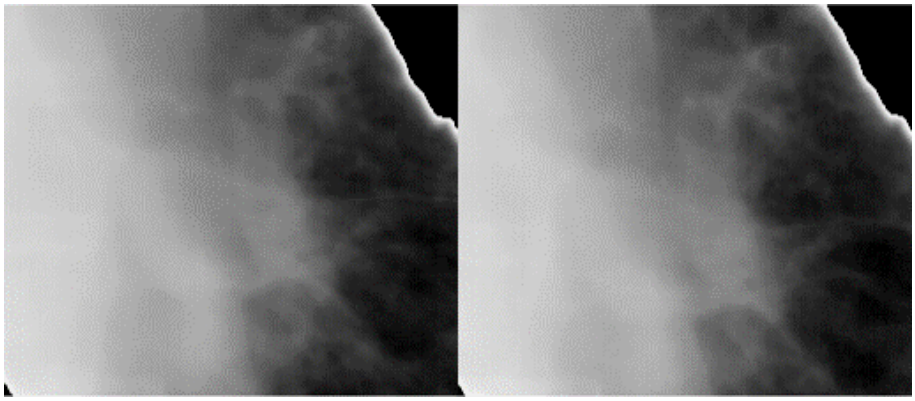

(a) template of fraction 31 (left) and template found in fraction 32 (right)

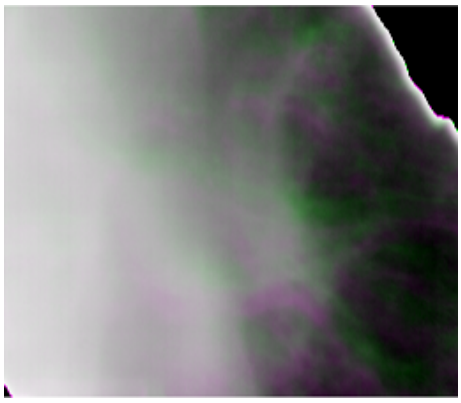

(b) overlay of the two templates, showing a mismatch of the tumour in CC direction

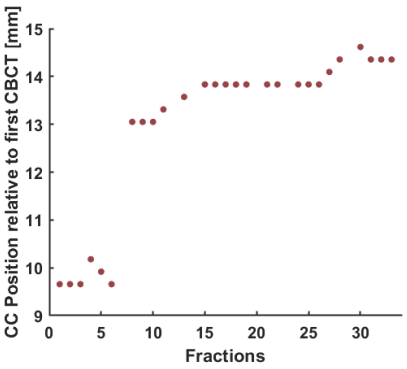

(c) segmented position for all fractions

Figure 2.11: Patient 8 Field 1: a case where the edge of the field was in the template frame and the algorithm locked onto it in several cases such as from fraction 15 to 26

Chapter 3

Results

3.1 Tumour segmentation

Table 3.1 shows the number of segmentable fields for the analysed patients. 76% (26/34) of fields where the GTV was in the field were well suited for segmentation. The reason for the tumour not being in some fields, is that these only irradiated the lymph node targets.

Patient	Total Fields	GTV in Field	Segmentable	% Segmentable
1	5	4	3	75%
2	4	4	3	75%
3	7	4	3	75%
4	6	5	4	80%
6	5	5	5	100%
8	6	6	4	67%
10	7	6	4	67%
Total	40	34	26	76%

Table 3.1: Number of segmentable fields per patient, where the last column represents the percentage of fields with the GTV that were segmentable

Figure 3.1 represents the difference in tumour position between what was intended by the RTT in the setup and where it was segmented in the MV image taken during treatment. In all patients there was a significant mean drift of the tumour 2.7 mm ($p<0.01$) in the cranial direction between the CBCT and the delivery of the first segmented field, ranging from 0.3 to 5.2 mm. In Patients 1, 3, 6 and 10 an addidional drift of the tumour from the first segmented field to the last was observed, which also resulted in a significant drift after the first field over all patients with a mean of 1.43 mm ($p<0.01$).

Table 3.2 shows the mean positions for the first and last field per patient. The drift was calculated for the mean over all fractions (weighted mean drift), and for individual fractions (unweighted mean drift). They were found to be in the order of 1.4 – 1.6 mm. This is also reflected in the box plots in Fig. 3.3 where

Patient	mean first	mean last	mean drift
1	2.35	3.39	1.04
2	3.13	3.39	0.26
3	2.09	4.44	2.35
4	3.13	4.57	1.44
6	0.26	3.26	3.00
8	5.22	4.70	-0.52
10	1.44	6.00	4.57
weighted mean	2.67	4.25	1.58
unweighted mean	2.73	4.16	1.43

Table 3.2: Mean segmented CC position of first and last segmented fields and the calculated drift in [mm]. The weighted mean is calculated from the means of the patients, the unweighted mean from the individual fractions

(a) shows the segmented CC position in all first fields vs what was segmented in the last field and (b) visualizes the drift on the means of all patients.

In Figure 3.2 the first versus last segmented positions of each fraction are plotted together for each patient to see if the trend persists within a single fraction. The diagonal line represents equal position in both fields and therefore data points above represent fractions where there was a drift in cranial direction during the treatment. In patients 3, 6, and 10 95% of data points represent fractions with cranial drift, whereas for other patients no significant drift tendency can be seen.

To summarise, a cranial tumour drift occurred in all patients in the time between the setup CBCT and delivery of the first field and in some patients even continued throughout the treatment.

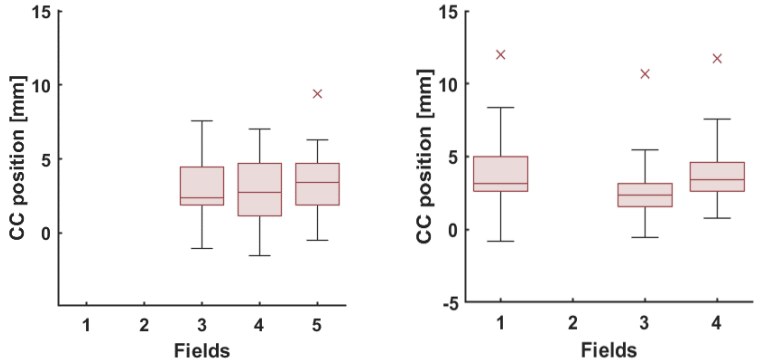

(a) Patient 1

(b) Patient 2

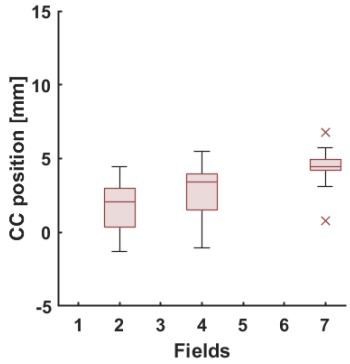

(c) Patient 3

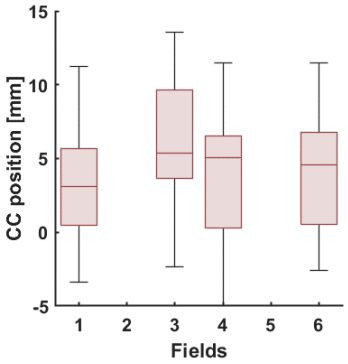

(d) Patient 4

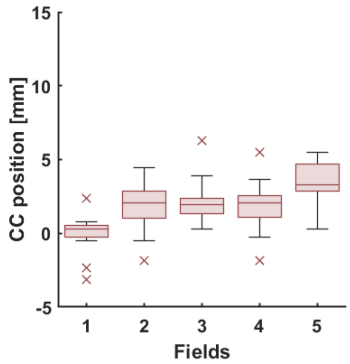

(e) Patient 6

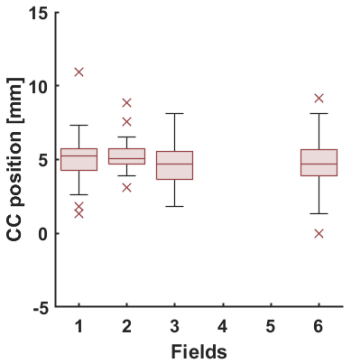

(f) Patient 8

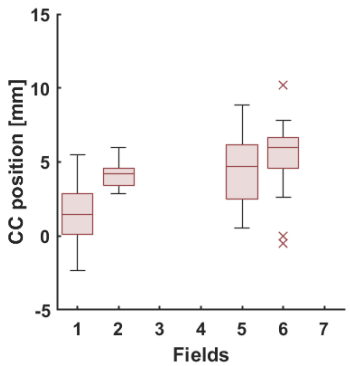

(g) Patient 10

Figure 3.1: Box plots for the segmented CC position of all fractions per field where the crosses are outliers, the whiskers represent the range of the data without outliers, the box shows the lower and upper quartiles and the mean is represented by the horizontal line

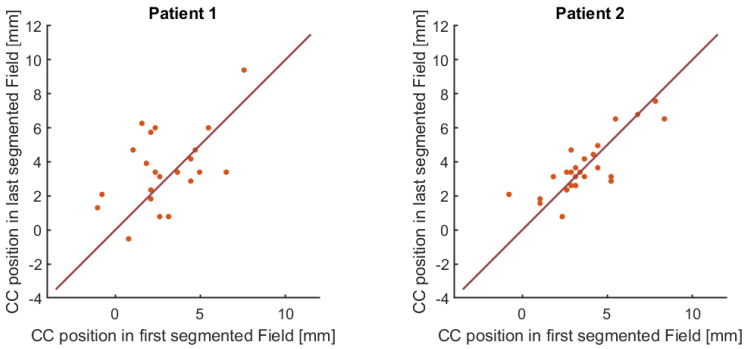

(a) Patient 1

(b) Patient 2

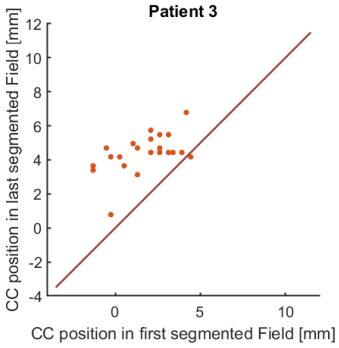

(c) Patient 3

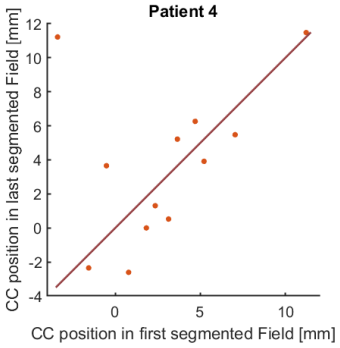

(d) Patient 4

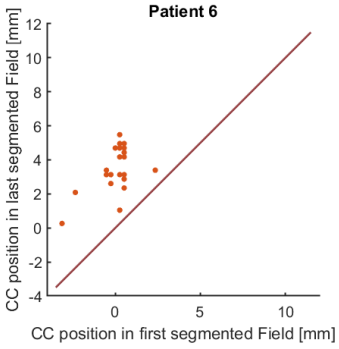

(e) Patient 6

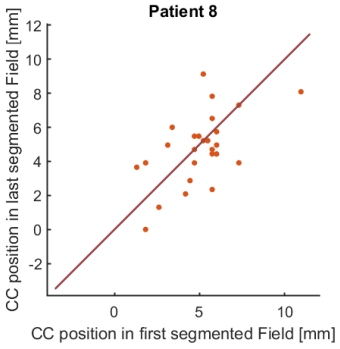

(f) Patient 8

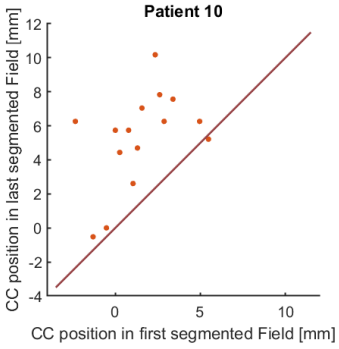

(g) Patient 10

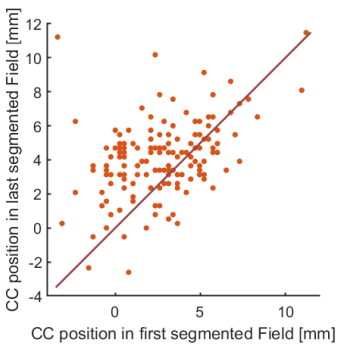

(h) all Patients

Figure 3.2: scatter plots of segmented CC position in first field vs last field for every fraction, diagonal line representing the same position in both images, (h) is a plot of all fractions of all segmented patients

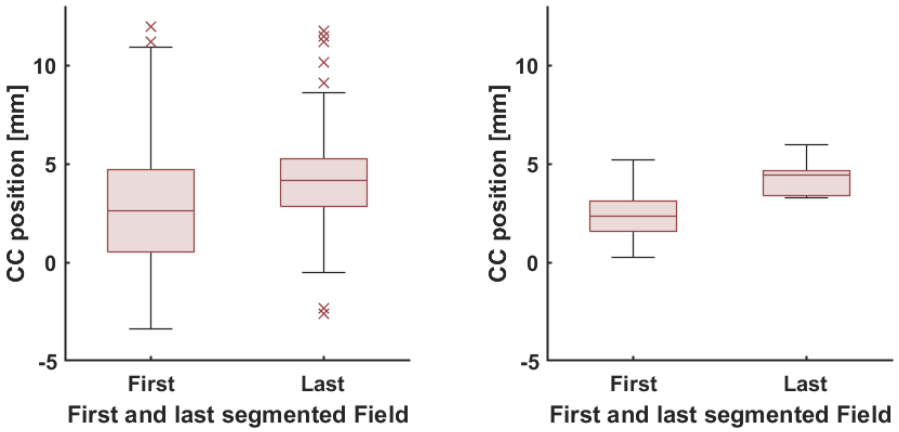

(a) for all individual fractions (b) drift on the mean of all patients

Figure 3.3: Drift in cranial direction from the first to the last segmented field in all patients

3.2 Non-segmentable patients and difficult cases

Patient	Reason segmentation failed
5	no cine MV
7	small GTV
9	bad contrast
11	no cine MV
12	small GTV
13	fields delivered in two DIBH

Table 3.3: Overview of the non-segmentable patients and why they could not be segmented

Table 3.3 shows all patients that could not be segmented. Patients 5 and 9 had no cine MV images available and were therefore not analysed.

Patient 7 This patient could not be segmented because the tumour structure was very small (1.58 cm^3) and therefore not visible in the MV images. Even in the teMV, the tumour was not distinguishable from blood vessels in the lung due to the edge being very blurry.

Patient 9 The GTV overlapped with either the diaphragm or the heart in most fields and where it did not, the edge of the aperture was very close to the tumour or even overlapping so that the tumour edge was not visible (this was planned in two of the fields). Therefore this patient was not suited for segmentation either.

Patient 12 Here the GTV was again very small (0.15 cm^3) and the enhancement procedure was not enough to make the teMV segmentable. Further, this set of cine MV images only consisted of 7 out of 30 fractions.

Patient 13 When analysing this patient, it became apparent that the fields had been delivered in two DIBH each. This resulted in motion artefacts in the MV images due to the diaphragm position changing, as can be seen in Figure 3.4. Even if the GTV could be segmented in the teMV images, the segmented position would come with additional uncertainties, since the cMV was created under the assumption that there is no tumour motion during field delivery. Additionally, the target overlapped with the diaphragm and/or the heart so that there was not enough contrast to make the structure visible.

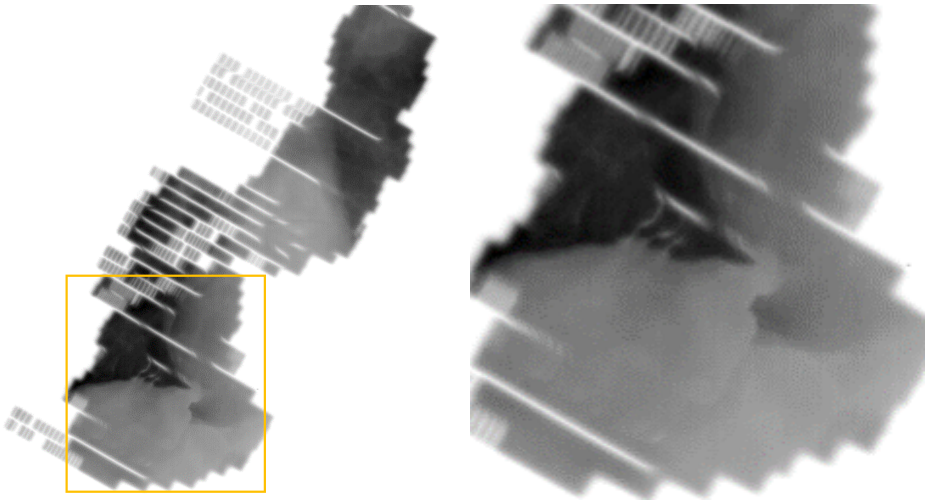

(a) Diaphragm motion artefact due to the field being delivered in 2 DIBH cycles

(b) closeup of the diaphragm as indicated in (a) by the rectangle

Figure 3.4: Example for motion artefacts, taken from Patient 13 Field 1

In conclusion, difficult cases for segmentation include the following:

- The enhancement procedure for small GTVs is very sensitive to motion, since artefacts can make the tumour unrecognisable in the teMV image after subtraction, as the wrong information may get subtracted.
- Artefacts in the CBCT (DRRs) or cMV images
- Low tumour contrast, for example when the tumour is not surrounded by lung tissue in the projection
- GTV that overlaps with the diaphragm or is close to the field edge, as can be seen in Figure 3.5 where segmentation was not possible with the *rectangular* mask (green) due to overlapping with the edge and containing

the diaphragm. However, it was possible to segment the tumour with the GTV conformal mask (white), as the disturbing areas were cut from the template.

- Difference in tumour appearance in DRR_{tumour} and teMV as can be seen in Figure 3.6. This is usually connected to low tumour contrast in the cMV image before subtraction. The template based segmentation depends on the shape of the tumour being similar, therefore this impacts the performance of the algorithm negatively.

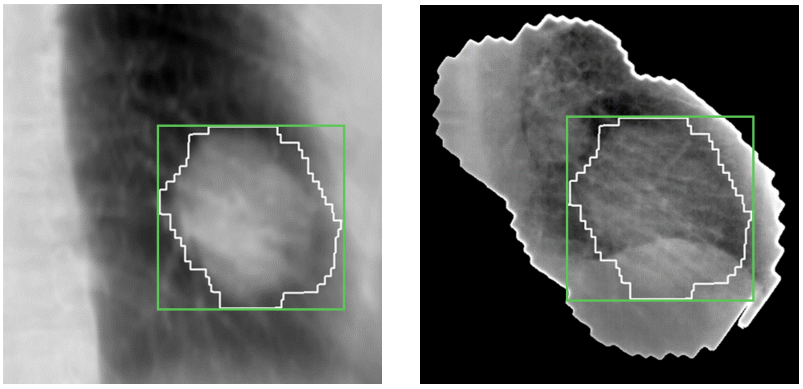

(a) GTV conformal template in DRR_{tumour}

(b) GTV conformal template segmented in teMV image

Figure 3.5: Patient 1, Field 5: an example for a case where template matching with the GTV conformal mask (white) made segmentation possible even though the diaphragm was overlapping with the template. Segmentation with the rectangular template (green) was not possible.

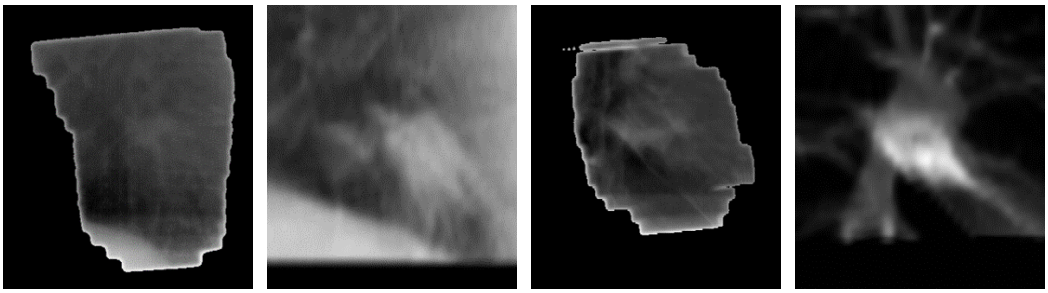

(a) Patient 4, Field 5 teMV image

(b) Patient 4, Field 5 DRR_{tumour}

(c) Patient 10, Field 4 teMV image

(d) Patient 10, Field 4 DRR_{tumour}

Figure 3.6: Cases where the appearance of the tumour structure (in the centre in all images) in the teMV and the DRR template was very different

3.3 3D position estimate

Figure 3.7 shows the 3D position estimations calculated from all segmented positions in a fraction. The box plots are divided into the individual patients and LR, CC and AP directions each, where left, cranial and anterior are represented by the positive direction and right, caudal and posterior by the negative direction on the vertical axis. While the tumour position is relatively stable in the LR direction, it can be seen that there is a systematic drift in the cranial direction, accompanied by a smaller posterior drift.

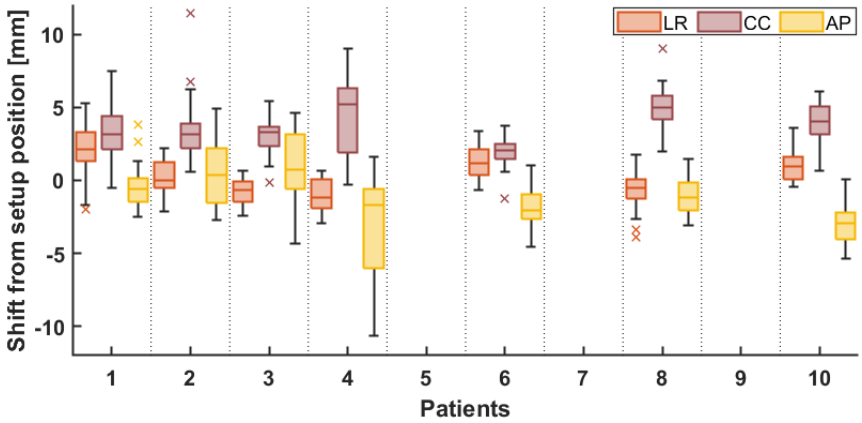

Figure 3.7: estimated 3D position for all Patients over all fractions in LR, CC and AP direction

3.4 PTV Margins

Table 3.4 shows the setup margins calculated from the estimated tumopur motion in 3D. The individual directions are then visualized in Figure 3.8 with the corresponding PTV margins shifted by the mean value M. The mean positions in CC (3.5 mm) and AP (-1.2 mm) direction were significantly different from zero ($p<0.01$).

The calculated margins in CC direction is smaller than what is used in the clinic, however, the large shift found in CC direction is not included in the clinically applied setup margins. The margins in LR direction are very similar. Surprisingly, the margin in the AP direction is bigger than the one used in the clinic, which is dominated by a big Σ (standard deviation of the means) in this direction.

	CC [mm]	LR [mm]	AP [mm]
Mean	3.5*	0.3	-1.2*
Σ	1.0	1.2	1.6
σ	1.9	1.2	2.1
$2.5\Sigma + 0.7\sigma$	3.8	3.9	5.5
PTV margin in the clinic	5.0	4.0	4.0

Table 3.4: Setup margins calculated for all three directions compared to the PTV margins used in the clinic.
* mean significant from zero ($p<0.01$)

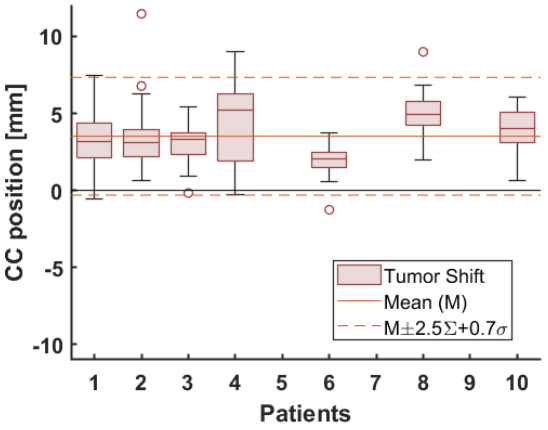

(a) estimated CC positions and PTV margin

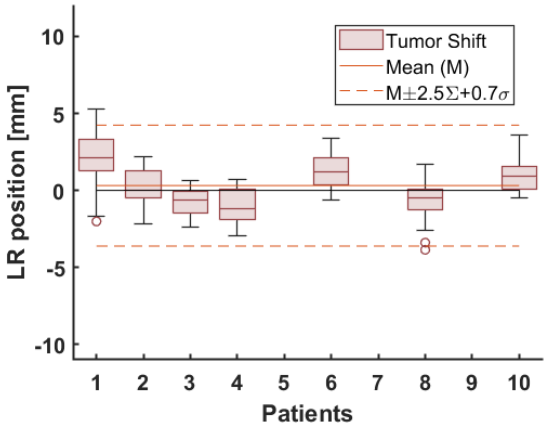

(b) estimated LR positions and PTV margin

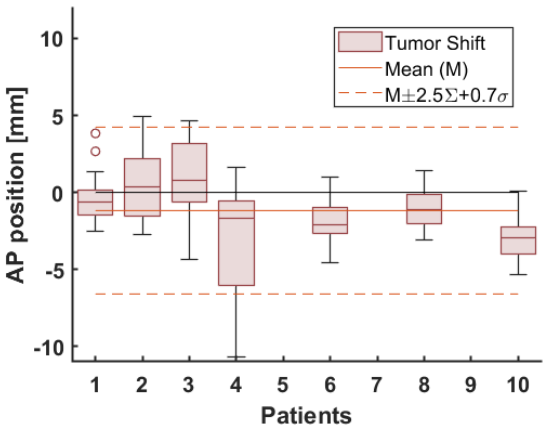

(c) estimated AP positions and PTV margin

Figure 3.8: Box plots for the estimated positions in each CC, LR and AP directions and their respective margin shifted by the mean M

Chapter 4

Discussion

4.1 Subjective setup position

When analysing the intrafraction tumour shifts, it is important to notice that they are relative to the daily setup position. The match made on the tumour is decided by the RTT, it may be different from day to day, and includes some subjectivity. It is especially difficult to evaluate the match when there is tumour shrinkage, since it might not shrink isotropically in all directions and the invisible tumour spread still needs to be irradiated. This is a very important aspect of motion management in lung cancer radiotherapy.

Therefore, it can only be determined how well the RTT's choice of position can be reproduced during field delivery, and we have not yet found a method to directly compare them to each other or to the treatment plan. This is where the MV-MV cross-correlation would have been useful, had it worked. Since this is not possible, it might be wise to use the template-based segmentation on the DRRs from fraction to fraction to compare how the setup match varies and relate this directly to the planning CT. This position may then also be used to calculate the interfraction motion on the MV images.

4.2 Artefacts

Artefacts in the images can greatly affect the performance of the algorithm. They can occur in both the DRR projections of the CBCT and the cMV images. Artefacts in the setup CBCT can arise due to the scan being taken in sections during three separate DIBH, which may result in a change of position of the imaged organs. This negatively affects the tumour template quality by blurring the edge of the tumour structure (Fig. 4.1 a).

In cMV images, artefacts occur mostly due to movement of the MLC over the field, which may cause artefacts in two cases: Firstly, when neighbouring leaves

Patients	artefacts present	artefacts over GTV
1 - 13	49 (80%)	9 (14%)
analysed	25 (75%)	2 (6%)

Table 4.1: Fields where artefacts from fast-moving MLC leaves were present and in how many cases they crossed over the GTV, for all patients and only the seven analysed patients

don't sweep over the field at the same time. This leads to a stripe artefact between the two, caused by the penumbra of the photon beam (Fig. 4.1 b). As long as only one of the images in the cross-correlation has the stripe artefact, the impact on the segmentation is minimal; the cross-correlation value will be lower, but the algorithm will return the same position as without the stripe artefact. A way to remove the stripes might be to look up the MLC movements in the plan and correct for the penumbra by increasing the intensity in the affected area.

Secondly, when MLC leaf pairs move over the field very fast with a small gap, which causes small rectangular artefacts along the path of the leaves (Fig. 4.1 c and d). This mostly happens at the field edge and when they sweep over areas that have been prescribed less dose, such as the lymph nodes, since less exposure leads to less deposited dose. Therefore, these artefacts only affected the tumour segmentation in few cases (Table 4.1). But where they did cross over the GTV, segmentation failed. Increasing the frame rate of the frame grabber might help to reduce the occurrence of these artefacts.

4.3 DRR verification

It was central to align the setup CBCT and the cineMV images correctly to determine the relative position between them. The isocentres for the two usually do not match due to the couch shift initiated by the RTT's soft tissue match on the tumour. This couch shift was recorded and then applied in calculating the DRRs as described in Section 2.2.2, but the coordinate systems of different appliances may not be the same.

To verify that the couch shift was implemented correctly in the algorithm, the DRR_{total} was compared with the cMV image of the first fraction with an overlay. In most fields, the anatomy was the only indication of whether the match was correct, and there was no ground truth to be referred to. However, in some cMV images, the outlines of the respiratory motion monitoring block (RPM) that was used for gating the DIBH were visible (Fig. 4.2). Since the gating depends on the position of the RPM block, its position in both images should be similar and

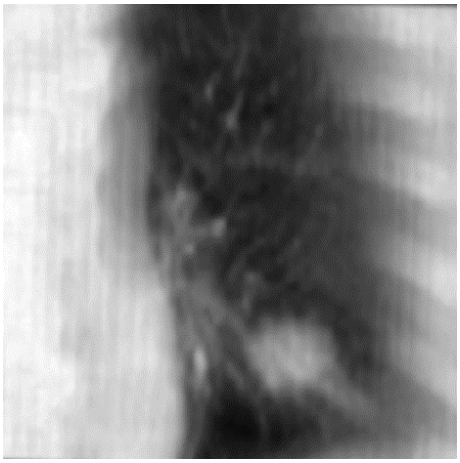

(a) Blurring in the DRR of Patient 4

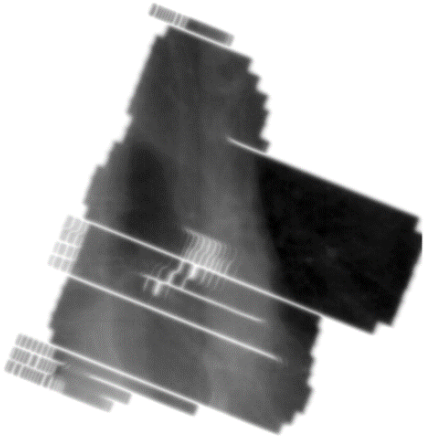

(b) stripe aftefacts in cMV of Patient 7 Field 2

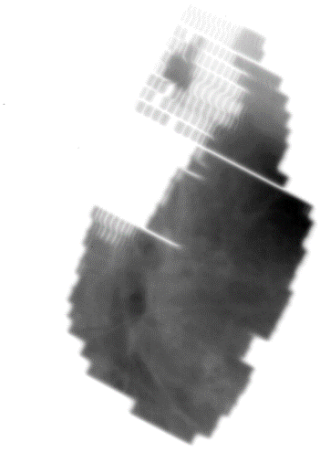

(c) Patient 7 Field 1

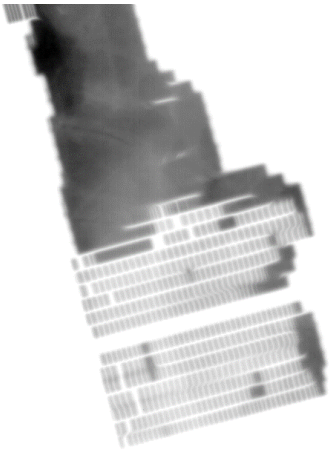

(d) Patient 13 Field 2

Figure 4.1: Artefacts in DRR and cMV images

can therefore be used as a measure of how accurate the match is. The outlines of the RPM block were sufficiently visible in both the DRR_{total} and the cMV images to verify the couch shift and were especially important to determine the correct rotational correction, which was not possible on just the anatomy, since the angle is usually small, in the order of 0.1°- 2°and this small change was easier to verify on a rectangular shape.

Naturally, this method is impacted by the intrafraction movement that is to be determined in this study and it is, therefore, difficult to determine the ground truth, especially since the RPM block is only visible in very few fields (5 Patients

with one field each). Experiments and measurements with a lung phantom would be useful for further verification.

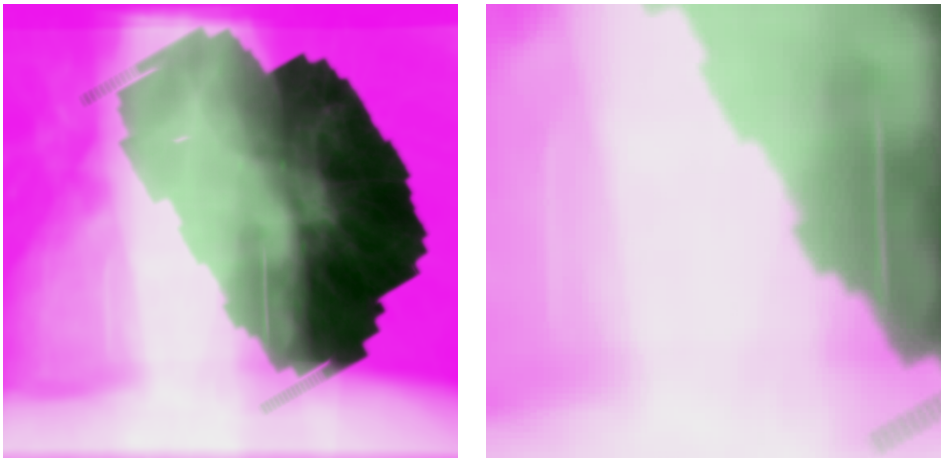

(a) DRR-cMV overlay

(b) closeup of a) showing the rectangular outline of the RPM block

Figure 4.2: verification of the couch shift applied to the CBCT for DRR calculation

4.4 Linear intensity fit and generating the teMV image

Adjusting the contrast in the DRRs with the linear fit was very effective and enhancing the contrast in the cMV by subtraction of $\mathrm{DRR}_{\text{non-tumour}}$ worked well. However, it may have been a better choice to fit the DRR to the logarithm of the cMV image instead, considering the physical property represented by the intensities of the DRR and cMV images. This may have resulted in a more accurate fit and made the subtraction factor in Eq. (2.7) redundant.

Another possible improvement on the DRR calculation is to change the way $\mathrm{DRR}_{\text{tumour}}$ and $\mathrm{DRR}_{\text{non-tumour}}$ are calculated. Using a simple slab around the tumour worked well but the segmentation may be improved by using the GTV in the structure file to cut away any structures outside the tumour that may still be in the tumour-containing slab, therefore improving the tumour template. However, using the GTV conformal mask on the $\mathrm{DRR}_{\text{tumour}}$ calculated with the slab as can be seen in Figure 3.5 had the same impact on the accuracy of the segmentation and the computation time was much shorter (recalculating the DRR for one patient over all fractions would take upwards of two hours).

4.5 Choice of template

The choice of template affects how well the tumour localisation algorithm works. Since the most important information about the tumour location in both the DRR and the teMV image is the edge of the tumour, it might make sense to force the algorithm to focus more on that. A way in which this was already done, is with the template shaped conformally to the GTV. An extension of this could be a ring shaped template, that contains only a band of the edge with a margin in both directions, therefore cutting out less important information such as the appearance of the inner part of the tumour, which might be different in each image.

4.6 Margins

The calculated PTV margin (Table 3.4) was smaller in the CC direction than what is currently used in the clinic, and the margin in AP direction was found bigger. However, the margins are certainly underestimating the errors, since the segmented positions are relative to the intended setup position. The subjectivity of the tumour match on the setup CBCT adds additional uncertainties that were not taken into account in this study. It would also be better to include more patients in the calculation of the margins.

Additionally, there is an inherent selection bias in the patients where the tumour was segmentable: GTVs close to the diaphragm have the biggest motion amplitude during a breathing cycle, and possibly also from one DIBH to another, but could not be segmented.

4.7 Cranial and posterior tumour drift

It has been shown in Section 3.1 that there is a significant drift in cranial direction before, as well as during treatment. In Section 3.4, the estimated 3D position showed an average cranial drift of (3.5 ± 2.0)mm (mean ± SD) relative to the tumour position in the setup CBCT , and a significant posterior drift of (1.2 ± 2.3)mm (Table 3.4).

This is in line with what other studies have found that investigated intrafraction motion during radiotherapy of lung and liver:

- Schmitt et al. [12] investigated intrafraction motion of the mediastinal lymph nodes in lung cancer patients. The study compared the motion of mediastinal lymph nodes between the setup CBCT and kV images during treatment delivery and found a baseline drift of (2.2 ± 1.8)mm in cranial

direction and (1.0 ± 1.2)mm in posterior direction.

- Guckenberger et al. [13] investigated intrafraction lung tumour motion by comparing the setup CBCT to a CBCT taken immediately after delivery of the last field. They found a an absolute 3D drift of the tumour with (2.8 ± 1.6)mm with a small systematic tumour drift of (1.3 ± 1.9)mm in posterior direction, which is comparable to the results of this study. However, the cranial tumour drift was only (0.6 ± 1.5)mm.

- Worm et al. [14] investigated the intrafraction motion of liver tumours during gated stereotactic body radiotherapy (SBRT) guided by implanted electro magnetic transponders. Gating also used a couch shift to correct for drifts. In nongated treatments, a cranial drift of (2.2 ± 1.8)mm and a posterior drift of (0.9 ± 0.9)mm were found, where most of the drift occurred before delivery of the first field. This is in line with the results of this study, it seems that liver tumours have a similar drifting motion to lung tumours.

A possible explanation for this significant mean cranial drift during treatment is the following hypothesis: while the patient is upright, gravity is pulling their organs downwards, which changes direction when the patient lays down. Therefore, the organs slowly drift towards the head over the time of the treatment. Additionally, the mean shift of 1.2 mm in the posterior direction supports this hypothesis, as it indicates the organs are now being pulled towards the back of the patient. If this was true, it would be a good solution to have the patient lie down for some time before imaging and treatment ($\sim$ 15 minutes). A trial with a control group could help verify that hypothesis.

Another possible cause is the internal target position and external gating signal not necessarily correlating: This hypothesis suggests, that patients become tired and breathe less deeply into the stomach with subsequent breath holds. This can happen since the gating only measures the movements of the chest, therefore, different depths of the breath-hold can result in a similar monitoring signal.

Chapter 5

Outlook

Due to the time constraint on this project, it was only possible to analyse seven patients. To calculate reliable margins on the PTV, the analysis of more patients is necessary. Some cases in the cohort were particularly interesting, such as patient 27: They had three separate tumour GTVs delineated, of which two seem easily segmentable. It would be interesting to segment them separately and investigate their relative intrafraction motion.

Possible extensions of the project beyond this thesis are as follows:

- Some patients in the cohort had their heart exposed to the beam and the heart motion is therefore visible in the cine MV images. Since the research group of Per Poulsen has previously developed an algorithm for fully automated heart dose calculation from cine MV images recorded during breast cancer treatments [15] it might be possible to also apply this to the cine MV images of lung cancer patients treated in DIBH.
- Further, the segmented positions in the individual fields could be used to estimate the dose actually delivered to the GTV, if they can be related to the planning CT directly.
- A marker segmentation algorithm has been used on the same cohort to analyse the intrafraction motion of the lymph node markers in the kV images taken during treatment. It might be possible to also use the MV images with the developed algorithm to segment the lymph nodes and compare the two.

Chapter 6

Conclusion

A method for markerless lung tumour localization in cine MV images was developed and successfully applied to 7 patients to determine the intrafraction tumour shift between setup imaging and treatment delivery in lung cancer DIBH IMRT treatments. Margins for the PTV were calculated from the segmented tumour positions during treatment and agree well with the PTV margins used in the clinical procedure at AUH. While calculating the margins, it was found that the position of the tumour is more cranial during the treatment than in the setup CBCT. To mitigate this drift during treatment, having the patients lie down for 15 minutes before imaging may be a good option.

During this study, a lot of knowledge was gained about template-based markerless tumour segmentation in MV images. Especially on what the conditions are for the template-based segmentation to work well:

- The contrast of the tumour to the surrounding lung tissue needs to be big enough ($\sim$50% of the edge or more has to be visible) as the edges are what is most important for template matching
- If the tumour is too small, generating a tumour enhanced MV image is difficult. Therefore, a certain size is required (> 1.6 cm^3)
- If the tumour is very close to other high-contrast structures, using a GTV-conformal template is beneficial.
- If the tumour overlaps with the diaphragm in the cine MV images, segmentation becomes very difficult due to the negative impact the non-rigidness of the diaphragm has on the tumour enhancing subtraction.
- Most importantly the shape and texture need to be similar in both the DRRs and the MV images. If this is not the case, it is very difficult to verify that the segmentation algorithm worked correctly.

Due to these criteria, segmentation failed for four patients. However, of the analysed treatments the tumour was segmentable in 76% of IMRT fields containing the GTV and a mean of 4 fields per patient were well suited for segmentation.

Bibliography

[1] "Danish comprehensive cancer center," 2022. [Online]. Available: https://www.dccc.dk/english/national-research-centres/danish-national-centre-for-lung-cancer-research/

[2] E. Jakobsen, T. R. Rasmussen, and A. Green, "Mortality and survival of lung cancer in denmark: Results from the danish lung cancer group 2000–2012," *Acta Oncologica*, vol. 55, pp. 2–9, 2 2016.

[3] F. M. Khan, "The physics of radiation therapy," 2014.

[4] E. B. Podgorsak and K. Kainz, *Radiation Oncology Physics: A Handbook for Teachers And Students*. International Atomic Energy Agency, 2005.

[5] D. A. Palma, S. Senan, K. Tsujino, R. B. Barriger, R. Rengan, M. Moreno, J. D. Bradley, T. H. Kim, S. Ramella, L. B. Marks, L. D. Petris, L. Stitt, and G. Rodrigues, "Predicting radiation pneumonitis after chemoradiation therapy for lung cancer: An international individual patient data meta-analysis," *International Journal of Radiation Oncology*Biology*Physics*, vol. 85, pp. 444–450, 2 2013.

[6] C. B. Simone, "Thoracic radiation normal tissue injury," *Seminars in Radiation Oncology*, vol. 27, pp. 370–377, 10 2017.

[7] M. Josipovic, "Phd thesis deep inspiration breath hold for radiotherapy for patients with lung cancer," 2018.

[8] MATLAB, *version 9.10.0.1739362 (R2021a)*. The MathWorks Inc., 2022.

[9] S. Skouboe, T. Ravkilde, J. Bertholet, R. Hansen, E. S. Worm, C. G. Muurholm, B. Weber, M. Høyer, and P. R. Poulsen, "First clinical real-time motion-including tumor dose reconstruction during radiotherapy delivery," *Radiotherapy and Oncology*, vol. 139, pp. 66–71, 10 2019.

[10] M. V. Herk, P. Remeijer, and J. V. Lebesque, "The probability of correct target dosage: Dose-population histograms for deriving treatment margins in radiotherapy," 2000.

[11] M. V. Herk, "Errors and margins in radiotherapy," *Seminars in Radiation Oncology*, vol. 14, pp. 52–64, 2004.

[12] M. L. Schmidt, L. Hoffmann, D. S. Møller, M. M. Knap, T. R. Rasmussen, B. H. Folkersen, and P. R. Poulsen, "Systematic intrafraction shifts of mediastinal lymph node targets between setup imaging and radiation treatment

delivery in lung cancer patients," *Radiotherapy and Oncology*, vol. 126, pp. 318–324, 2 2018.

[13] M. Guckenberger, J. Meyer, J. Wilbert, A. Richter, K. Baier, G. Mueller, and M. Flentje, "Intra-fractional uncertainties in cone-beam ct based image-guided radiotherapy (igrt) of pulmonary tumors," *Radiotherapy and Oncology*, vol. 83, pp. 57–64, 4 2007.

[14] E. S. Worm, M. Høyer, R. Hansen, L. P. Larsen, B. Weber, C. Grau, and P. R. Poulsen, "A prospective cohort study of gated stereotactic liver radiation therapy using continuous internal electromagnetic motion monitoring," *International Journal of Radiation Oncology Biology Physics*, vol. 101, pp. 366–375, 6 2018.

[15] S. Andreasen, C. Muurholm, S. Skouboe, H. Spejlborg, B. Offersen, and P. Poulsen, "Oc-0224: Fully automated heart dose calculation from cine mv images recorded during breast cancer treatments," *Radiotherapy and Oncology*, vol. 152, pp. S114–S115, 11 2020.